

Published in final edited form as:

Neuroimage. 2012 February 1; 59(3): 2625–2635. doi:10.1016/j.neuroimage.2011.08.077.

MRI Estimates of Brain Iron Concentration in Normal Aging Using Quantitative Susceptibility Mapping

Berkin Bilgic^{a,*}, Adolf Pfefferbaum^{b,c}, Torsten Rohlfing^b, Edith V. Sullivan^c, and Elfar Adalsteinsson^{a,d}

^aDepartment of Electrical Engineering and Computer Science, Massachusetts Institute of Technology, USA

^bNeuroscience Program, SRI International, USA

^cDepartment of Psychiatry and Behavioral Sciences, Stanford University School of Medicine, USA

^dHarvard-MIT Division of Health Sciences and Technology, Massachusetts Institute of Technology, USA

Abstract

Quantifying tissue iron concentration *in vivo* is instrumental for understanding the role of iron in physiology and in neurological diseases associated with abnormal iron distribution. Herein, we use recently-developed Quantitative Susceptibility Mapping (QSM) methodology to estimate the tissue magnetic susceptibility based on MRI signal phase. To investigate the effect of different regularization choices, we implement and compare ℓ_1 and ℓ_2 norm regularized QSM algorithms. These regularized approaches solve for the underlying magnetic susceptibility distribution, a sensitive measure of the tissue iron concentration, that gives rise to the observed signal phase. Regularized QSM methodology also involves a pre-processing step that removes, by dipole fitting, unwanted background phase effects due to bulk susceptibility variations between air and tissue and requires data acquisition only at a single field strength. For validation, performances of the two QSM methods were measured against published estimates of regional brain iron from *postmortem* and *in vivo* data. The *in vivo* comparison was based on data previously acquired using Field-Dependent Relaxation Rate Increase (FDRI), an estimate of MRI relaxivity enhancement due to increased main magnetic field strength, requiring data acquired at two different field strengths. The QSM analysis was based on susceptibility-weighted images acquired at 1.5T, whereas FDRI analysis used Multi-Shot Echo-Planar Spin Echo images collected at 1.5T and 3.0T. Both datasets were collected in the same healthy young and elderly adults. The *in vivo* estimates of regional iron concentration comported well with published *postmortem* measurements; both QSM approaches yielded the same rank ordering of iron concentration by brain structure, with the lowest in white matter and the highest in globus pallidus. Further validation was provided by comparison of the *in vivo* measurements, ℓ_1 -regularized QSM versus

© 2011 Elsevier Inc. All rights reserved.

*Correspondence to: Berkin Bilgic, Massachusetts Institute of Technology, Room 36-776A, 77 Massachusetts Avenue, Cambridge, MA 02139, berkin@mit.edu, Fax: 617-324-3644, Phone: 617-866-8740.

Conflict of interest statement

Drs. Bilgic, Pfefferbaum, Rohlfing, Sullivan have no conflicts of interest with this work, either financial or otherwise. Author Adalsteinsson receives research support from Siemens Healthcare and the Siemens-MIT Alliance.

Publisher's Disclaimer: This is a PDF file of an unedited manuscript that has been accepted for publication. As a service to our customers we are providing this early version of the manuscript. The manuscript will undergo copyediting, typesetting, and review of the resulting proof before it is published in its final citable form. Please note that during the production process errors may be discovered which could affect the content, and all legal disclaimers that apply to the journal pertain.

FDRI and ℓ_2 -regularized QSM versus FDRI, which again yielded perfect rank ordering of iron by brain structure. The final means of validation was to assess how well each *in vivo* method detected known age-related differences in regional iron concentrations measured in the same young and elderly healthy adults. Both QSM methods and FDRI were consistent in identifying higher iron concentrations in striatal and brain stem ROIs (i.e., caudate nucleus, putamen, globus pallidus, red nucleus, and substantia nigra) in the older than in the young group. The two QSM methods appeared more sensitive in detecting age differences in brain stem structures as they revealed differences of much higher statistical significance between the young and elderly groups than did FDRI. However, QSM values are influenced by factors such as the myelin content, whereas FDRI is a more specific indicator of iron content. Hence, FDRI demonstrated higher specificity to iron yet yielded noisier data despite longer scan times and lower spatial resolution than QSM. The robustness, practicality, and demonstrated ability of predicting the change in iron deposition in adult aging suggest that regularized QSM algorithms using single-field-strength data are possible alternatives to tissue iron estimation requiring two field strengths.

Keywords

Susceptibility mapping; Normal aging; Brain; Iron

Introduction

Excessive iron deposition in subcortical and brain stem nuclei occurs in a variety of degenerative neurological and psychiatric disorders, including Alzheimer's disease, Huntington's Chorea, multiple sclerosis, and Parkinson's disease (Hallgren and Sourander, 1960). Further, *postmortem* (Hallgren and Sourander, 1958) and *in vivo* (Bartzokis et al., 2007b; Haacke et al., 2007; Pfefferbaum et al., 2009; Pfefferbaum et al., 2010; Raz et al., 2007) studies have revealed that deep gray matter brain structures accumulate iron at different rates throughout adult aging. Structures that exhibit iron accrual support components of cognitive and motor functioning (Bartzokis et al., 2010; Raz et al., 2007; Sullivan et al., 2009). To the extent that excessive iron presence may attenuate neuronal function or disrupt connectivity, quantification and location of iron deposition may help explain age- and disease-related motor slowing and other selective cognitive decline.

Several MRI methods have been proposed for *in vivo* iron mapping and quantification. Bartzokis et al. (Bartzokis et al., 1993) capitalized on the enhanced transverse relaxivity (R_2) due to iron with increasing main field strength for the Field-Dependent Relaxation Rate Increase (FDRI) method. FDRI relies on the use of R_2 -weighted imaging at two different field strengths and attributes the relaxation enhancement at higher field to iron, which may be a specific measure of tissue iron stores (Bartzokis et al., 1993).

Whereas FDRI relies on the modulation of signal intensity in MRI to infer iron concentration, MRI signal phase has also been proposed as a source signal for iron mapping, both by direct evaluation of phase images (Haacke et al., 2005a; Haacke et al., 2004) and by reconstruction of magnetic susceptibility images that derive from the phase data (Haacke et al., 2007; Haacke et al., 2005a). Local iron concentration is strongly correlated with the magnetic susceptibility values (Duyn et al., 2007; Liu et al., 2010c; Schweser et al., 2011b); therefore, quantification of this paramagnetic property presents a sensitive estimate of iron concentration, although possibly complicated by more uncommon factors, such as pathological manganese deposition (Hazell and Butterworth, 1999). Phase mapping yields high-resolution, high-SNR data that demonstrate correlation with iron (Haacke et al., 2007), but as an estimate of the underlying magnetic susceptibility, it suffers from non-local effects and spatial modulation artifacts due to the non-trivial mapping from susceptibility to phase

(de Rochefort et al., 2010). To overcome these limitations, we made use of regularized Quantitative Susceptibility Mapping (QSM) algorithms that robustly estimate the magnetic susceptibility χ of tissues based on gradient-echo signal phase. The magnetic susceptibility χ maps to the observed phase shift in MRI via a well-understood transformation, but the inverse problem, i.e., estimation of χ from phase, is ill posed due to zeros on a conical surface in the Fourier space of the forward transform; hence, χ inversion benefits from additional regularization. Recently, elegant regularization methods were proposed for deriving susceptibility inversion. In the work by de Rochefort et al. (2010), smooth regions in the susceptibility map are promoted to match those of the MR magnitude image by introducing a weighted ℓ_2 norm penalty on the spatial gradients of χ . Likewise, Liu et al. (2010a) regularized the inversion by minimizing the ℓ_1 norm of gradients of χ , again weighted with a mask derived from the image magnitude. Kressler et al. (2010) experimented using ℓ_1 and ℓ_2 norm regularizations directly on the susceptibility values, rather than posing the minimization on the gradient coefficients. Another method to stabilize the susceptibility reconstruction problem is to acquire data at multiple orientations and invert them simultaneously *without* regularization. This approach was introduced by Liu et al. (2009) and also investigated by others such as Wharton and Bowtell (2010) and Schweser et al. (2011b).

In this work, we investigate two different regularization schemes for susceptibility inversion; using ℓ_1 -regularized QSM that parallels the approach of Liu et al. (2010a) and ℓ_2 -regularized QSM which was introduced by de Rochefort et al. (2010). Given that magnetic susceptibility is a property of the underlying tissue, in ℓ_1 -regularized QSM we make the assumption that it is approximately constant within regions of the same tissue type or within an anatomical structure. Based on this premise, the ℓ_1 -norm-penalized QSM algorithm regularizes the inversion by requiring the estimated χ to be sparse in the image gradient domain. On the other hand, placing an ℓ_2 norm penalty on the spatial gradients of χ does not promote sparsity, but results in a large number of small gradient coefficients and thus incurs a smooth susceptibility reconstruction. In addition to regularized susceptibility inversion, our approach incorporates a robust background phase removal technique based on effective dipole fitting (Liu et al., 2010b), which addresses the challenging problem of removing phase variations in the data that arise primarily from bulk susceptibility variations between air and tissue rather than the more subtle changes of χ within the brain. Dipole fitting contains no parameters that need tuning and preserves the phase variations caused by internal susceptibility effects more faithfully than high-pass filtering, as employed in susceptibility-weighted imaging (SWI) (Haacke et al., 2005a; Haacke et al., 2004). All susceptibility mapping methods require data acquired at only one field strength, thereby overcoming certain limitations of the FDRI approach, including long scan times and the need for spatial registration of image data acquired with different scanners at different field strengths.

Here, we describe the ℓ_1 and ℓ_2 norm regularized QSM methods and apply them to SWI data previously acquired in groups of younger and elderly, healthy adults (Pfefferbaum et al., 2009). To validate the iron measures, we compared the results of QSM methods with values published from a *postmortem* study (Hallgren and Sourander, 1958). As further validation, we compared QSM results with those based on FDRI collected in the same adults (Pfefferbaum et al., 2009) to test the hypothesis that the iron deposition in striatal and brain stem nuclei, but not white matter or thalamic tissue, would be greater in older than younger adults.

Methods

Susceptibility and MR signal phase

The normalized magnetic field shift δ measured in a gradient-echo sequence is related to the MR image phase ϕ via $\delta = -\phi/(B_0 \cdot \gamma \cdot TE)$, where B_0 is the main magnetic field strength, γ is the gyromagnetic ratio, and TE is the echo time. It follows from Maxwell's magnetostatic equations that the relationship between the underlying susceptibility distribution χ and the observed field shift δ is given by (de Rochefort et al., 2010; Marques and Bowtell, 2005; Salomir et al., 2003)

$$\mathbf{F} \delta = \left(\frac{1}{3} - \frac{k_z^2}{k_x^2 + k_y^2 + k_z^2} \right) \circ \mathbf{F} \chi \quad (1)$$

where \mathbf{F} is the discrete Fourier transform matrix, k_x and k_y are the in-plane frequency indices, k_z is the frequency index along B_0 , and \circ denotes Hadamard (element-wise) multiplication. Denoting with \mathbf{D} the kernel that relates the field map to the susceptibility, the relation can also be expressed as

$$\delta = \mathbf{F}^{-1} \mathbf{D} \mathbf{F} \chi \quad (2)$$

The spatial frequencies at which the kernel is zero define a conical surface in k -space, which effectively undersamples the Fourier transform of χ and thereby gives rise to the ill-posed problem of susceptibility estimation from image phase. In addition, the susceptibility kernel is not defined at the center of k -space (the DC point), but one can choose a solution that vanishes at infinity, which is obtained by setting the Fourier transform of the field to 0 at $k = 0$ (de Rochefort et al., 2010). This assignment of signal for the k -space origin causes the resulting χ to have zero mean; but independent of the particular design choice for this DC signal, the susceptibility distribution is inherently a spatial map of *relative* susceptibilities. Under the assumption that the field map and the susceptibility distribution are differentiable along k_z , Li *et al.* (2011) derived that the convolution kernel equals $-2/3$ at $k = 0$. In this work, we adopt the convention of assigning 0 to the DC value of the kernel. Thus, to achieve absolute quantification of χ , some reference value needs to be established. For this study, we chose the magnetic susceptibility value in splenium as a reference. This structure was preferred over taking as a reference the CSF, for which the susceptibility values were observed to differ substantially between the anterior and the posterior ventricles in this study.

Background effect removal from the field map

In addition to the relatively subtle internal effects of the tissue iron on the MRI phase, background artifacts caused by air-tissue boundaries contribute the vast majority of signal variation in the observed phase. While the susceptibility difference between air and water is about 9.4 *ppm* (parts per million) (Schenck, 1996), the largest within-brain variation due to tissue iron is more than an order of magnitude smaller. Assuming that the average human tissue susceptibility is similar to that of water, it is clear that background effects dominate the observed phase and this undesired signal component is a challenge to robust susceptibility inversion. Because the background effects usually vary slowly across space, various methods have been proposed to filter them out based on this frequency characteristic, such as polynomial fitting (Duyn et al., 2007) and forward modeling to

estimate the phase from the air/tissue interface (Neelavalli et al., 2009). Even though these methods are effective for background phase removal, their impact on the internal phase variations due to tissue iron is unclear. A recent background field removal algorithm, *effective dipole fitting* (Liu et al., 2010b), aims to estimate the background susceptibility distribution that optimally matches the field inside the region of interest (ROI), and removes this contribution to recover the foreground field map. This is achieved by solving a least-squares problem

$$\chi_{out} = \operatorname{argmin}_{\chi} \|\mathbf{M}\delta - \mathbf{F}^{-1}\mathbf{D}\mathbf{F}\tilde{\mathbf{M}}\chi\|_2^2 \quad (3)$$

where \mathbf{M} is the brain mask that marks the ROI and $\tilde{\mathbf{M}}$ is the complement of \mathbf{M} , thus marking the background. After solving for χ_{out} , the field map induced only by the internal local effects is obtained by

$$\delta_{in} = \delta - \mathbf{F}^{-1}\mathbf{D}\mathbf{F}\tilde{\mathbf{M}}\chi_{out} \quad (4)$$

Compared with high-pass filtering, effective dipole fitting was seen to yield 1/3 to 1/7 times the root-mean-square error relative to the true field maps obtained from reference scans (Liu et al., 2010b). Another elegant background removal technique called SHARP (Schweser et al., 2011b), with results comparable to those of the dipole fitting method (Schweser et al., 2011a), involves removing the harmonic contributions to the phase inside the region of interest by filtering.

Susceptibility inversion with ℓ_1 regularization

The final step in the proposed algorithm is to estimate the susceptibility distribution that gives rise to δ_{in} . Hence, we seek to solve

$$\delta_{in} = \mathbf{F}^{-1}\mathbf{D}\mathbf{F}\chi_{in} \quad (5)$$

Because some of the spatial frequencies are undersampled by the kernel \mathbf{D} , the inversion of χ_{in} benefits from regularization that imposes prior knowledge on the reconstructed susceptibility map. The susceptibility values are tied to the paramagnetic properties of the underlying tissue structure; hence they vary smoothly across space within anatomical boundaries and can be approximated to be piece-wise constant. In this case, the susceptibility map is expected to be sparsely represented in the spatial image gradient domain. To formulate this belief, we seek the χ distribution that matches the field map δ_{in} , and that also has sparse image gradients

$$\chi_{in} = \operatorname{argmin}_{\chi} \|\delta_{in} - \mathbf{F}^{-1}\mathbf{D}\mathbf{F}\chi\|_2^2 + \lambda \cdot \|\mathbf{G}\chi\|_1 \quad \text{with} \quad \mathbf{G} = \begin{bmatrix} \mathbf{G}_x \\ \mathbf{G}_y \\ \mathbf{G}_z \end{bmatrix} \quad (6)$$

where $\|\mathbf{G}\chi\|_1$ is the ℓ_1 norm of image gradients in all three dimensions, and λ is a regularization parameter that trades off data consistency and spatial smoothness. This convex program is very similar to the objective function in the Compressed Sensing (CS)

MRI literature, where the aim is to reconstruct MR images from undersampled k -space data. According to CS theory, if the underlying image can be approximated to be sparse in a transform domain, then it can be recovered from randomly undersampled k -space data via a nonlinear recovery scheme, and the reconstruction quality depends on the number of observed frequency samples as well as the coherence of the aliasing artifacts in the transform domain (Lustig et al., 2007). The nonlinear recovery method usually involves penalizing the ℓ_1 norm of the transformed image. Based on this, Eq. 6 can be viewed as CS reconstruction with a modified observation matrix \mathbf{DF} instead of the undersampled Fourier transform.

An objective function similar to Eq. 6 has been previously proposed in Liu et al. (2010a), which included a smoothing term of the form $\|\mathbf{W}_G \mathbf{G} \chi\|_L$. Here, \mathbf{W}_G is a weighting matrix derived from the MRI image magnitude, and L denotes the choice of the norm, which can be either ℓ_1 or a homotopic approximation to the ℓ_0 norm. Apart from the magnitude weighting, our method parallels this approach.

Susceptibility inversion with ℓ_2 regularization

Another way of introducing regularization to the inversion problem is by penalizing the ℓ_2 norm of spatial gradients of the susceptibility distribution,

$$\chi_{in} = \operatorname{argmin}_{\chi} \|\delta_{in} - \mathbf{F}^{-1} \mathbf{DF} \chi\|_2^2 + \beta \cdot \|\mathbf{G} \chi\|_2^2 \quad (7)$$

In contrast with the ℓ_1 regularization that promotes sparse spatial gradients (i.e. a small number of non-zero gradient coefficients), ℓ_2 -regularized inversion favors a large number of small gradient coefficients. Regularized QSM with ℓ_2 norm penalty was introduced in de Rochefort et al. (2010), which also included a weighting matrix \mathbf{W}_1 derived from the signal magnitude in the regularization term to yield $\|\mathbf{W}_1 \mathbf{G} \chi\|_2^2$. To investigate the effect of the regularization norm selection in susceptibility inversion, we present QSM results with both regularization styles.

Effect of regularization parameters λ and β

The regularization parameter λ in Eq. 6 determines the smoothness of the reconstructed susceptibility map such that larger values of λ yield smoother image results than do smaller ones (Fig. 1). This flexibility allows us to control the scale of spatial features present in the χ reconstruction. In terms of imposing prior belief on the susceptibility distribution, it is possible to recover Eq. 6 by assuming that the normalized field map δ_m is corrupted by white Gaussian noise with some variance σ^2 and by placing a sparsity-promoting Laplacian prior distribution on the gradient coefficients of the χ map,

$$p \partial \chi = \left(\frac{\lambda}{4\sigma^2} \right)^M \exp \left(- \frac{\lambda}{2\sigma^2} \sum_{i=1}^M |\partial \chi_i| \right) \quad (8)$$

where $\partial \chi$ represents the spatial gradient of χ , and M is the total number of voxels in χ . With these noise and prior models, invoking the *maximum a posteriori* (MAP) estimate reduces to Eq. 6. From this point of view, using a large λ will produce a highly peaked prior distribution at zero, inducing sparser image gradient solutions, and smoother susceptibility maps.

Again from a Bayesian perspective, the ℓ_2 norm regularization corresponds to computing the MAP estimate after placing a multivariate Gaussian prior on the gradient coefficients of the susceptibility map,

$$p(\partial\chi) = \frac{1}{2\pi\sigma^2/\beta^{M/2}} \exp\left(-\frac{1}{2\sigma^2/\beta} \sum_{i=1}^M |\partial\chi_i|^2\right) \quad (9)$$

where σ^2 is the data noise in the field map and β is the regularization parameter in Eq. 7. Hence, the variance of the gradient coefficients σ^2/β is inversely proportional to the ℓ_2 regularization parameter β . Accordingly, a large regularization parameter will limit the variation in the gradient coefficients and induce smaller values (Fig. 2).

Selection of regularization parameters λ and β

To choose appropriate regularization parameters that balance data consistency and the amount of regularization, the L-curve method was employed (Hansen, 2000). The corners of the L-curves were not sharp for ℓ_1 - and ℓ_2 -regularized reconstructions (Figs. 1&2), and optimal regularization parameters were determined by finding the operating points with the largest curvature. L-curve tests were performed on a young and an elderly subject from the *in vivo* dataset and the optimal operating points were found to be $\lambda = 2 \cdot 10^{-4}$ for ℓ_1 -regularized QSM and $\beta = 1.5 \cdot 10^{-2}$ for ℓ_2 -regularized reconstructions on both the young and the elderly subjects.

Dataset acquired in younger and elderly adults used for comparison of regularized QSM and FDRI

To examine consistency with our previous study that investigated the performance of FDRI (Pfefferbaum et al., 2009), we tested our new iron quantification algorithm on the same dataset, as summarized below.

Subjects

Two groups of healthy, highly educated, right-handed adults were studied: 11 younger adults (mean \pm S.D. age = 24.0 \pm 2.5, range = 21 to 29 years, 15.9 years of education; 5 men, 6 women) and 12 elderly adults (mean \pm S.D. age = 74.4 \pm 7.6, range = 64 to 86 years, 16.3 years of education; 6 men, 6 women). The younger subjects included laboratory members and volunteers recruited from the local community. All older participants were recruited from a larger ongoing study of normal aging and scored well within the normal range on the Dementia Rating Scale (Mattis, 1988): mean = 140.6, range = 132 to 144 out of 144, cutoff for dementia = 124. Mean (and range) of days between 1.5T and 3.0T scan acquisition were 16.5 (0 to 56) days for the young and 9.3 (0 to 42) days for the elderly group; for 2 of the young and 8 of the elderly both sets of scans were acquired on the same day.

Image acquisition protocols

MRI data were acquired prospectively on 1.5T and 3.0T General Electric (Milwaukee, WI) Signa human MRI scanners (gradient strength = 40 mT/m; slew rate = 150 T/m/s).

FDRI acquisition

At 1.5T, after auto shimming for the session, the following sequences were acquired for 62 axial slices, each 2.5 mm thick:

1. 3D SPOiled Gradient Recalled Echo (SPGR) for structural imaging and registration (TR/TE=8.1/3.3 ms, FA=30°);
2. multi-shot Echo Planar Spin Echo (EPSE) (TR/TE 6000/17, FA=90°, 256×192 in-plane, FOV=24 cm, 4 NEX, 24 interleaves with 8 phase-encode lines per TR, 9:40 min);
3. multi-shot EPSE (TR/TE 6000/60, FA=90°, 256×192 in-plane, FOV=24 cm, 6 NEX, 24 interleaves, 14:20 min).

At 3.0T, after auto shimming for the session, the following sequences were acquired in the axial plane:

1. 3D SPGR for structural imaging and registration (TR/TE=8.1/3.3 ms, FA=15°, 124 slices, 1.25 mm thick);
2. multi-shot EPSE (TR/TE 6000/17, FA=90°, 256×192 in-plane, FOV=24 cm, 3 NEX, 24 interleaves, 62 slices, 2.5 mm thick, 7:10 min);
3. multi-shot EPSE (TR/TE 6000/60 ms, FA=90°, 256×192 in-plane, FOV=24 cm, 6 NEX, 24 interleaves, 62 slices, 2.5 mm thick, 14:20 min).

Susceptibility-Weighted Image acquisition

At 1.5T, after auto shimming for the session, the following sequences were acquired for 62 axial slices, each 2.5 mm thick:

1. 3D SPGR for structural imaging and registration (TR/TE=28/10 ms, FA=30°, 256×256 in-plane, 24 cm FOV);
2. susceptibility-weighted 3D SPGR (TR/TE=58 ms/40 ms, FA=15°, 512×256 in-plane, 24 cm FOV, 12:20 min, with flow compensation) (Haacke et al., 2007; Haacke et al., 2005b);
3. 2D gradient-recalled echo sequence (TR/TE=600/3 ms, FA=20°);
4. 2D gradient-recalled echo sequence (TR/TE=600/7 ms, FA=20°).

Phase images were constructed from the real and imaginary components of the SWI-SPGR data after the phase had been unwrapped with FSL PRELUDE (Phase Region Expanding Labeler for Unwrapping Discrete Estimates (Jenkinson, 2003)). The magnitude and phase-unwrapped SWI data were down-sampled from 512×256 to 256×256 via averaging to match the FDRI resolution. Brain masks were generated with the FSL Brain Extraction Tool, BET (Smith, 2002), to be used in the dipole fitting step for background phase removal. After estimating the foreground field maps from the unwrapped phase data with the down-sampled size 256×256, susceptibility maps were generated with the two QSM algorithms.

Image registration

As previously described (Pfefferbaum et al., 2009), for each subject and for 1.5T and 3.0T separately, the late-echo EPSE data were nonrigidly registered (Rohlfing and Maurer, 2003) [<http://nitrc.org/projects/cmtk/>] to the early-echo EPSE data. This was necessary because the two echoes arose from separate acquisitions, rather than a single dual-echo acquisition, and were, therefore, not always perfectly aligned with each other. The 1.5T early-echo EPSE image of each subject was registered to the 3.0T early-echo EPSE image of the same subject, which was then registered nonrigidly to the subject's 3.0T SPGR image. The 3.0T SPGR image from each subject, after brain extraction using BET, finally was registered nonrigidly to the SPGR channel of the SRI24 atlas (Rohlfing et al., 2010) [<http://nitrc.org/projects/sri24/>]. Via concatenation of the aforementioned registration

transformations, the 1.5T and 3.0T early-echo and late-echo images were all reformatted into 1-mm isotropic SRI24 space, each using a single interpolation with a 5-pixel-radius cosine-windowed sinc kernel. Reformatting both 1.5T and 3.0T data from each subject into SRI24 coordinates via that subject's 3.0T SPGR image (rather than separately via the early-echo EPSE images at each field strength) ensures that the unavoidable inter-subject registration imperfections are consistent for images from both field strengths. The 1.5T SWI magnitude images were rigidly registered to a contemporaneously acquired structural SPGR image, which was then registered nonrigidly to the same subject's 3.0T SPGR image. The SWI-SPGR registration was limited to a rigid transformation because signal dropouts in magnitude SWI due to B0 field inhomogeneities prevented nonrigid correction of the relatively small distortions between SWI and SPGR. Again, via concatenation of transformations, the phase images were reformatted into SRI24 space, again with a 5-pixel radius cosine sinc kernel. All data were analyzed in common 1-mm isotropic SRI24 atlas space.

Region-of-Interest (ROI) identification

Voxel-by-voxel FDRI images ($FDRI=(R_{23T}-R_{21.5T})/1.5T$) were created for each subject and used to make a group FDRI average, comprising all young and elderly subjects. A similar group average was made for the QSM images, and separate young and elderly group averages were made for display purposes (Fig. 3).

As previously described (Pfefferbaum et al., 2009), bilateral caudate, globus pallidus, putamen, thalamus, and white matter sample regions of interest (ROIs) were drawn (by A.P.) on the group-average (all young plus all elderly subjects) FDRI images in common SRI24 space, reformatted in the coronal plane. The globus pallidus, putamen, caudate, and white matter sample were drawn on 10 contiguous, 1-mm thick slices at an anterior-posterior location that maximized the presence of all three basal ganglia structures in the same slices. The thalamus was drawn on the next 10 contiguous slices posterior to the basal ganglia. The caudate was eroded one pixel and thalamus was eroded two pixels on a slice-by-slice basis to avoid partial voluming of CSF. Substantia nigra and red nucleus ROIs were also identified, based on their FDRI intensities. The same ROIs were also manually identified on the group-average phase data (all young and all elderly combined), reformatted in the *axial* plane (Ogg et al., 1999), and guided by phase conspicuity. When drawing ROIs on the phase data, an effort was made to exclude the bright rims around the globus pallidus and putamen as well as the division between them. Although this approach biases the data towards more negative phase (i.e., lower values reflecting less iron), its purpose was to maximize the sensitivity of phase to age effects. Thus, iron estimates were conducted on both sets of ROI identifications, the phase-guided and the FDRI-guided.

For each subject and for each ROI at each field strength, the mean intensity of all voxels in an ROI for the early- and late-echo EPSE were used to compute R_{23T} and $R_{21.5T}$ and the FDRI. QSM values were computed as the magnetic susceptibility in parts per million (ppm) for all voxels identified in each ROI projected onto each individual's QSM dataset. Thus, both FDRI intensity and phase conspicuity were each used to guide ROI delineation. The average susceptibility of splenium in each subject was used as a reference for that subject's reported QSM results. This was preferred over taking the CSF susceptibility as a reference, as it was seen to differ substantially between the anterior and the posterior regions. Although the raw averages in the splenium did not differ significantly between the young and the elderly groups ($p=0.2359$ for ℓ_1 -regularized and $p=0.2016$ for ℓ_2 -regularized QSM), they were larger in the elderly group than the young group ($\chi_{splenium}^{elderly} = -0.0378$ ppm and $\chi_{splenium}^{young} = -0.0479$ ppm for ℓ_1 -regularized and $\chi_{splenium}^{elderly} = -0.0297$ ppm and

$\chi_{\text{splenium}}^{\text{young}} = -0.0374$ ppm for ℓ_2 -regularized QSM). This should induce a bias *against* observing young-elderly group susceptibility differences in the regularized QSM reconstructions.

Statistical analysis

We predicted that the ROI iron values would correlate positively with published *postmortem* iron values (Hallgren and Sourander, 1958) and with FDRI values. Comparisons of the two *in vivo* iron indices with each other and also with published *postmortem* values were based on nonparametric (Spearman) correlations. We then tested the hypotheses that, relative to the young group, the elderly group would have higher QSM and FDRI values in striatal and brain stem ROIs, but not in thalamic or white matter ROIs. Because we posed directional hypotheses, group differences were considered significant at $p \leq 0.0125$, the one-tailed, family-wise Bonferroni-corrected p -value at $\alpha = 0.05$ for 8 measures. All measurements were conducted twice: once with FDRI-guided ROI identification, and once with phase-guided ROI identification.

Results

Correlations of FDRI and QSM values with postmortem iron concentrations

Fig. 4 presents the mean \pm SD iron concentration determined *postmortem* in each ROI (Hallgren and Sourander, 1958) on the x -axis and the mean \pm SD FDRI values in s^{-1}/Tesla and ℓ_1 -regularized QSM values in ppm for young plus elderly subjects on the y -axis. The correlations between ℓ_1 -regularized QSM and *postmortem* ($Rho = 0.881$, $p = 0.0198$), between ℓ_2 -regularized QSM and *postmortem* ($Rho = 0.881$, $p = 0.0198$), and between FDRI and *postmortem* iron indices ($Rho = 0.952$, $p = 0.0117$) were high.

Correlations between in vivo QSM and FDRI iron concentration metrics

To investigate the consistency between the iron concentrations predicted by the two QSM methods and FDRI, we correlated the three metrics in each ROI belonging to the 23 subjects. The correlation parameters indicate strong agreement between ℓ_1 -regularized QSM and FDRI ($Rho = 0.976$, $p = 0.0098$) (Fig. 5) and between ℓ_2 -regularized QSM and FDRI ($Rho = 0.976$, $p = 0.0098$) (not shown).

Age differences in regional iron concentration: QSM and FDRI

All ROI and statistical analyses were conducted on both phase-guided and FDRI-guided ROIs. Based on the initial FDRI data analysis, which reported lack of consistent cerebral hemisphere asymmetries across iron-rich structures (Pfefferbaum et al., 2009), all analyses herein used bilateral data, expressed as the mean of the left and right measures for each ROI (Table 1). The three methods produced essentially the same results. All t -test and p -values are presented in Table 1.

Age differences identified with regularized QSM

Analysis of the QSM results indicated that the elderly group had significantly more iron than the young group in striatal regions of the putamen and globus pallidus for both ℓ_1 - and ℓ_2 -norm regularized results. Even though the elderly tended to have more iron in the caudate nucleus than the young, the difference was not significant in either of the QSM methods. Likewise, ℓ_1 - and ℓ_2 -regularized QSM values indicated significantly more iron in the elderly than young group in the red nucleus and substantia nigra, but not the dentate nucleus. The only exception was the ℓ_1 -regularized substantia nigra results on the phase-guided ROIs, for which the group difference was not significant using family-wise Bonferroni correction

Average susceptibility values in the thalamus tended to be lower in the elderly relative to the young (indicating less iron in the elderly group) for both types of regularization, and this difference was significant for ℓ_2 norm regularized QSM under phase-guided ROIs. Likewise, the elderly had smaller susceptibility values in the white matter sample, but the difference was not significant (Fig. 6).

Age differences identified with FDRI

The elderly group had a significantly higher FDRI than the young group in the putamen but not the caudate nucleus or the very iron-rich globus pallidus. Although the elderly tended to have higher FDRI values in the red nucleus and substantia nigra, the differences were not significant; the groups did not differ significantly in FDRI of the dentate nucleus. By contrast, the FDRI values in the thalamic and white matter samples were significantly lower (indicative of less iron) in the elderly than the young group (Fig. 6).

Discussion

This study presented regularized QSM methods with two different choices of regularization, namely ℓ_1 and ℓ_2 norm penalties, for quantifying susceptibility-weighted imaging data, and established their ability to measure iron concentration in regional striatal and brain stem nuclei of young and elderly adults. The *in vivo* estimates of regional iron concentration comported well with published *postmortem* measurements (Hallgren and Sourander, 1958), with both approaches yielding the same rank ordering of iron concentration by brain structure, from lowest in white matter to highest in globus pallidus. Further validation was provided by comparison of the *in vivo* measurements, the two QSM methods and FDRI, which again yielded perfect rank ordering of iron by structure. The final means of validation was to assess how well each *in vivo* method detected known age-related differences in regional iron concentrations measured in the same young and elderly healthy adults. Results from all three methods were consistent in identifying higher iron concentrations in striatal and brain stem ROIs (i.e., caudate nucleus, putamen, globus pallidus, red nucleus and substantia nigra) in the older than the young group. With the exception of ℓ_1 -regularized results for the substantia nigra averaged under phase-guided ROIs, QSM values in the globus pallidus, red nucleus and substantia nigra were significantly larger in the elderly than the young based on both FDRI- and phase-guided ROIs using ℓ_1 or ℓ_2 regularization. For the FDRI metric, significant difference was observed only in the putamen for FDRI- and phase-guided delineation. Therefore, QSM appeared more sensitive than FDRI in detecting age differences in brain stem structures by producing much smaller *p*-values in the statistical tests. Although both measurement approaches identified the globus pallidus as being the most iron-rich structure regardless of age, only QSM found that the concentration in the elderly was significantly higher than that in the young adults. The average susceptibility value in the globus pallidus of young subjects has been reported to be around 0.20 ppm by several groups, e.g. (Schweser et al., 2011b; Wharton and Bowtell, 2010) (taking CSF as reference, with isotropic voxels), which is larger than the group averages reported in this study (0.10 – 0.14 ppm, taking splenium as reference). This difference might stem from averaging across subjects and partial volume issues considering the 2.5 mm slice thickness used in data acquisition.

The two regularized QSM methods produced iron concentration estimates consistent with the well-established FDRI metric. In addition to yielding strongly correlated results to both FDRI and *postmortem* data, the susceptibility mapping approach possesses several other favorable qualities. First, the data acquisition step for QSM is completed at a single field strength, whereas acquisitions at two field strengths are required to compute the FDRI values. Working at a single field strength also eliminates the need for spatial registration, and thus a potential source of measurement error. Second, the susceptibility maps estimated

with the QSM algorithms have a higher spatial resolution than the FDRI images. This has the additional benefit of enabling the quantification of vessel oxygenation ratios, because the individual vessels can be clearly resolved in the produced χ maps. However, the presented QSM algorithms produce relative maps of tissue susceptibility, which requires the selection of a reference susceptibility value for absolute quantification. In this study, the average susceptibility of splenium in each subject was taken as reference, but a point to note is that white matter samples have been reported to have anisotropic susceptibility (Lee et al., 2010), i.e., their susceptibility values depend on the orientation relative to the main magnetic field.

The regularized QSM algorithms can be considered a refinement of the pioneering work by Haacke (Haacke et al., 2007; Haacke et al., 2005a; Haacke et al., 2004) on Susceptibility-Weighted Imaging (SWI), which estimates local iron concentration by inspecting the changes in gradient-echo image phase. Because the background phase constitutes the major part of the observed phase, high-pass filtering is applied to obtain an estimate of the phase accrued by the tissue iron while removing the slowly-varying background effects. Although practical, filtering also removes some tissue phase information (Liu et al., 2010b).

The proposed method addresses this problem by using an optimization approach called *dipole fitting* (Liu et al., 2010b) that estimates and subtracts the background phase without affecting the tissue phase. In addition to yielding high-quality tissue field maps, dipole fitting only requires the solution of a least-squares problem, which can be done using a variety of gradient or conjugate direction optimization methods. As opposed to the high-pass filtering approach, which requires optimal selection of filter size, and polynomial fitting, which depends on the order of the polynomial, dipole fitting contains no parameters that need tuning. On the other hand, high-pass filtering methods are dramatically faster than iterative optimization methods employed in the dipole fitting approach. In addition, rather than relying only on the image phase, which produces a spatially distorted measure of tissue iron concentration, the proposed method solves for the underlying paramagnetic property of the tissue and produces a regularized measure of χ , which in turn is a sensitive estimate of iron concentration.

Other susceptibility mapping algorithms have demonstrated robust results. An elegant approach by Schweser et al. (2011b) estimated the χ distribution without employing regularization. This approach, however, requires data to be acquired at three different orientations with respect to the main magnetic field, thereby providing challenges to subjects in terms of scan time and head positioning and challenges to post-acquisition processing in terms of spatial registration. Another influential QSM algorithm using regularization was introduced by de Rochefort et al. (2010) and it forms the basis of the ℓ_2 -regularized method used in our work. After obtaining the tissue field map by solving a least squares problem similar to the dipole fitting formulation of Liu et al. (2010b), this QSM algorithm places a weighted ℓ_2 norm penalty on the spatial gradients of χ . We believe that posing the reconstruction problem with an ℓ_1 norm penalty that promotes sparsity in the spatial gradient domain of the susceptibility distribution is a better fit to the nature of the problem. As the susceptibility kernel effectively undersamples the k -space of the tissue field map, the inversion problem is inherently an under-determined system similar to the one encountered in the compressed-sensing literature (Lustig et al., 2007). The demonstrated ability of sparsity-inducing priors in undersampled image reconstruction makes the ℓ_1 norm an excellent candidate for susceptibility mapping (Liu et al., 2010a), and the ℓ_1 -regularized algorithm in our study parallels this effort. We also note an interesting comparison in (Wharton and Bowtell, 2010) between the ℓ_2 -regularized approach similar to that of (de Rochefort et al., 2010) against a multiple-orientation reconstruction strategy. These results indicate that ℓ_2 -regularized single-orientation susceptibility maps yield iron estimates of quality comparable to those calculated using data acquired at multiple orientations.

Conclusion

Herein are presented two regularized Quantitative Susceptibility Mapping algorithms, employing ℓ_1 and ℓ_2 norm regularization, which successfully remove background phase effects via dipole fitting and solve for the tissue susceptibility distribution via convex optimization. The performance of these algorithms was favorable when compared with other published *in vivo* and *postmortem* estimates of regional tissue iron concentrations. Because the accumulation of iron in the brain can have untoward effects on motor and cognitive function in normal aging (Bartzokis et al., 2010; Sullivan et al., 2009) and can be disproportionately greater in degenerative diseases (Bartzokis et al., 1999; Bartzokis et al., 2007a; Bartzokis and Tishler, 2000; Brass et al., 2006; Granholm et al., 1993; Martin et al., 1998; Michaeli et al., 2007), quantitative assessment of this accumulation has the potential of providing a tool for monitoring or even diagnosis. The robustness, practicality, and demonstrated ability of predicting the change in iron deposition in adult aging suggest that the presented QSM algorithms using single-field-strength data is a possible alternative for FDRI tissue iron estimation requiring two field strengths.

Acknowledgments

National Institutes of Health, Grant numbers NIH R01 EB007942, AG019717, AA005965, AA017168, EB008381; National Science Foundation (NSF), Grant number 0643836; Siemens Healthcare; Siemens-MIT Alliance; MIT-CIMIT Medical Engineering Fellowship.

Abbreviations

MRI	Magnetic Resonance Imaging
QSM	Quantitative Susceptibility Mapping
FDRI	Field-Dependent Relaxation Rate Increase
FSE	fast spin echo
ROI	region-of-interest, ppm, parts per million
SWI	Susceptibility-weighted imaging

References

- Bartzokis G, Aravagiri M, Oldendorf WH, Mintz J, Marder SR. Field dependent transverse relaxation rate increase may be a specific measure of tissue iron stores. *Magnetic Resonance in Medicine*. 1993; 29:459–464. [PubMed: 8464361]
- Bartzokis G, Cummings JL, Markham CH, Marmarelis PZ, Treciokas LJ, Tishler TA, Marder SR, Mintz J. MRI evaluation of brain iron in earlier- and later-onset Parkinson's disease and normal subjects. *Magn Reson Imaging*. 1999; 17:213–222. [PubMed: 10215476]
- Bartzokis G, Lu PH, Tingus K, Mendez MF, Richard A, Peters DG, Oluwadara B, Barrall KA, Finn JP, Villablanca P, Thompson PM, Mintz J. Lifespan trajectory of myelin integrity and maximum motor speed. *Neurobiol Aging*. 2010; 31:1554–1562. [PubMed: 18926601]
- Bartzokis G, Lu PH, Tishler TA, Fong SM, Oluwadara B, Finn JP, Huang D, Bordelon Y, Mintz J, Perlman S. Myelin Breakdown and Iron Changes in Huntington's Disease: Pathogenesis and Treatment Implications. *Neurochem Res*. 2007a; 32:1655–1664. [PubMed: 17484051]
- Bartzokis G, Tishler TA. MRI evaluation of basal ganglia ferritin iron and neurotoxicity in Alzheimer's and Huntington's disease. *Cell Mol Biol (Noisy-le-grand)*. 2000; 46:821–833. [PubMed: 10875443]
- Bartzokis G, Tishler TA, Lu PH, Villablanca P, Altshuler LL, Carter M, Huang D, Edwards N, Mintz J. Brain ferritin iron may influence age- and gender-related risks of neurodegeneration. *Neurobiol Aging*. 2007b; 28:414–423. [PubMed: 16563566]

- Brass SD, Chen NK, Mulkern RV, Bakshi R. Magnetic resonance imaging of iron deposition in neurological disorders. *Top Magn Reson Imaging*. 2006; 17:31–40. [PubMed: 17179895]
- de Rochefort L, Liu T, Kressler B, Liu J, Spincemaille P, Lebon V, Wu JL, Wang Y. Quantitative Susceptibility Map Reconstruction from MR Phase Data Using Bayesian Regularization: Validation and Application to Brain Imaging. *Magnetic Resonance in Medicine*. 2010; 63:194–206. [PubMed: 19953507]
- Duyn JH, van Gelderen P, Li TQ, de Zwart JA, Koretsky AP, Fukunaga M. High-field MRI of brain cortical substructure based on signal phase. *Proceedings of the National Academy of Sciences of the United States of America*. 2007; 104:11796–11801. [PubMed: 17586684]
- Granhölm E, Bartzokis G, Asarnow RF, Marder SR. Preliminary associations between motor procedural learning, basal ganglia T2 relaxation times, and tardive dyskinesia in schizophrenia. *Psychiatry Res*. 1993; 50:33–44. [PubMed: 8511222]
- Haacke EM, Ayaz M, Khan A, Manova ES, Krishnamurthy B, Gollapalli L, Ciulla C, Kim I, Petersen F, Kirsch W. Establishing a baseline phase behavior in magnetic resonance imaging to determine normal vs. abnormal iron content in the brain. *Journal of Magnetic Resonance Imaging*. 2007; 26:256–264. [PubMed: 17654738]
- Haacke EM, Cheng NY, House MJ, Liu Q, Neelavalli J, Ogg RJ, Khan A, Ayaz M, Kirsch W, Obenaus A. Imaging iron stores in the brain using magnetic resonance imaging. *Magnetic Resonance Imaging*. 2005a; 23:1–25. [PubMed: 15733784]
- Haacke EM, Chengb NYC, House MJ, Liu Q, Neelavalli J, Ogg RJ, Khan A, Ayaz M, Kirsch W, Obenaus A. Imaging iron stores in the brain using magnetic resonance imaging. *Magnetic Resonance Imaging*. 2005b; 23:1–25. [PubMed: 15733784]
- Haacke EM, Xu Y, Cheng YC, Reichenbach JR. Susceptibility weighted imaging (SWI). *Magn Reson Med*. 2004; 52:612–618. [PubMed: 15334582]
- Hallgren B, Sourander P. The effect of age on the non-haemin iron in the human brain. *Journal of Neurochemistry*. 1958; 3:41–51. [PubMed: 13611557]
- Hallgren B, Sourander P. The non-haemin iron in the cerebral cortex in Alzheimer's disease. *J Neurochem*. 1960; 5:307–310. [PubMed: 14399117]
- Hansen PC. The L-Curve and its Use in the Numerical Treatment of Inverse Problems. *Computational inverse problems in electrocardiology*. 2000:119–142.
- Hazell AS, Butterworth RF. Hepatic encephalopathy: An update of pathophysiologic mechanisms. *Proc Soc Exp Biol Med*. 1999; 222:99–112. [PubMed: 10564534]
- Jenkinson M. Fast, automated, N-dimensional phase-unwrapping algorithm. *Magnetic Resonance in Medicine*. 2003; 49:193–197. [PubMed: 12509838]
- Kressler B, de Rochefort L, Liu T, Spincemaille P, Jiang Q, Wang Y. Nonlinear regularization for per voxel estimation of magnetic susceptibility distributions from MRI field maps. *IEEE Trans Med Imaging*. 2010; 29:273–281. [PubMed: 19502123]
- Lee J, Shmueli K, Fukunaga M, van Gelderen P, Merkle H, Silva AC, Duyn JH. Sensitivity of MRI resonance frequency to the orientation of brain tissue microstructure. *Proc Natl Acad Sci U S A*. 2010; 107:5130–5135. [PubMed: 20202922]
- Li W, Wu B, Liu C. Quantitative susceptibility mapping of human brain reflects spatial variation in tissue composition. *Neuroimage*. 2011; 55:1645–1656. [PubMed: 21224002]
- Liu, J.; Liu, T.; de Rochefort, L.; Khalidov, I.; Price, M.; Wang, Y. Quantitative susceptibility mapping by regulating the field to source inverse problem with a sparse prior derived from the Maxwell Equation: validation and application to brain. *International Society for Magnetic Resonance in Medicine 18th Scientific Meeting*; 2010a.
- Liu, T.; Khalidov, I.; de Rochefort, L.; Spincemaille, R.; Liu, J.; Wang, Y. Improved background field correction using effective dipole fitting. *International Society for Magnetic Resonance in Medicine 18th Scientific Meeting*; 2010b.
- Liu, T.; Liu, J.; de Rochefort, L.; Ledoux, J.; Zhang, Q.; Prince, MR.; Wu, J.; Wang, Y. Measurement of iron concentration in human brain using Quantitative Susceptibility Mapping (QSM): correlation with age. *International Society for Magnetic Resonance in Medicine 18th Scientific Meeting*; 2010c.

- Liu T, Spincemaille P, de Rochefort L, Kressler B, Wang Y. Calculation of Susceptibility Through Multiple Orientation Sampling (COSMOS): A Method for Conditioning the Inverse Problem From Measured Magnetic Field Map to Susceptibility Source Image in MRI. *Magnetic Resonance in Medicine*. 2009; 61:196–204. [PubMed: 19097205]
- Lustig M, Donoho D, Pauly JM. Sparse MRI: The application of compressed sensing for rapid MR imaging. *Magnetic Resonance in Medicine*. 2007; 58:1182–1195. [PubMed: 17969013]
- Marques JP, Bowtell R. Application of a fourier-based method for rapid calculation of field inhomogeneity due to spatial variation of magnetic susceptibility. *Concepts in Magnetic Resonance Part B-Magnetic Resonance Engineering*. 2005; 25B:65–78.
- Martin WR, Roberts TE, Ye FQ, Allen PS. Increased basal ganglia iron in striatonigral degeneration: in vivo estimation with magnetic resonance. *Can J Neurol Sci*. 1998; 25:44–47. [PubMed: 9532280]
- Mattis, S. *Psychological Assessment Resources*. Odessa, FL: 1988. Dementia rating scale.
- Michaeli S, Oz G, Sorce DJ, Garwood M, Ugurbil K, Majestic S, Tuite P. Assessment of brain iron and neuronal integrity in patients with Parkinson's disease using novel MRI contrasts. *Mov Disord*. 2007; 22:334–340. [PubMed: 17149719]
- Neelavalli J, Cheng YCN, Jiang J, Haacke EM. Removing Background Phase Variations in Susceptibility-Weighted Imaging Using a Fast, Forward-Field Calculation. *Journal of Magnetic Resonance Imaging*. 2009; 29:937–948. [PubMed: 19306433]
- Ogg RJ, Langston JW, Haacke EM, Steen RG, Taylor JS. The correlation between phase shifts in gradient-echo MR images and regional brain iron concentration. *Magn Reson Imaging*. 1999; 17:1141–1148. [PubMed: 10499676]
- Pfefferbaum A, Adalsteinsson E, Rohlfing T, Sullivan EV. MRI estimates of brain iron concentration in normal aging: Comparison of field-dependent (FDRI) and phase (SWI) methods. *Neuroimage*. 2009; 47:493–500. [PubMed: 19442747]
- Pfefferbaum A, Adalsteinsson E, Rohlfing T, Sullivan EV. Diffusion tensor imaging of deep gray matter brain structures: Effects of age and iron concentration. *Neurobiology of Aging*. 2010; 31:482–493. [PubMed: 18513834]
- Raz N, Rodrigue KM, Haacke EM. Brain aging and its modifiers: insights from in vivo neuromorphometry and susceptibility weighted imaging. *Ann N Y Acad Sci*. 2007; 1097:84–93. [PubMed: 17413014]
- Rohlfing T, Maurer CR Jr. Nonrigid image registration in shared-memory multiprocessor environments with application to brains, breasts, and bees. *IEEE Trans Inf Technol Biomed*. 2003; 7:16–25. [PubMed: 12670015]
- Rohlfing T, Zahr NM, Sullivan EV, Pfefferbaum A. The SRI24 multichannel atlas of normal adult human brain structure. *Human Brain Mapping*. 2010; 31:798–819. [PubMed: 20017133]
- Salomir R, De Senneville BD, Moonen CTW. A fast calculation method for magnetic field inhomogeneity due to an arbitrary distribution of bulk susceptibility. *Concepts in Magnetic Resonance Part B-Magnetic Resonance Engineering*. 2003; 19B:26–34.
- Schenck JF. The role of magnetic susceptibility in magnetic resonance imaging: MRI magnetic compatibility of the first and second kinds. *Medical Physics*. 1996; 23:815–850. [PubMed: 8798169]
- Schweser, F.; Atterbury, M.; Deistung, A.; Lehr, BW.; Sommer, K.; Reichenbach, JR. Harmonic phase subtraction methods are prone to B1 background components. *International Society for Magnetic Resonance in Medicine 19th Scientific Meeting*; 2011a.
- Schweser F, Deistung A, Lehr BW, Reichenbach JR. Quantitative imaging of intrinsic magnetic tissue properties using MRI signal phase: An approach to in vivo brain iron metabolism? *Neuroimage*. 2011b; 54:2789–2807. [PubMed: 21040794]
- Smith SM. Fast robust automated brain extraction. *Human Brain Mapping*. 2002; 17:143–155. [PubMed: 12391568]
- Sullivan EV, Adalsteinsson E, Rohlfing T, Pfefferbaum A. Relevance of Iron Deposition in Deep Gray Matter Brain Structures to Cognitive and Motor Performance in Healthy Elderly Men and Women: Exploratory Findings. *Brain Imaging Behav*. 2009; 3:167–175. [PubMed: 20161183]

Wharton S, Bowtell R. Whole-brain susceptibility mapping at high field: A comparison of multiple- and single-orientation methods. *Neuroimage*. 2010; 53:515–525. [PubMed: 20615474]

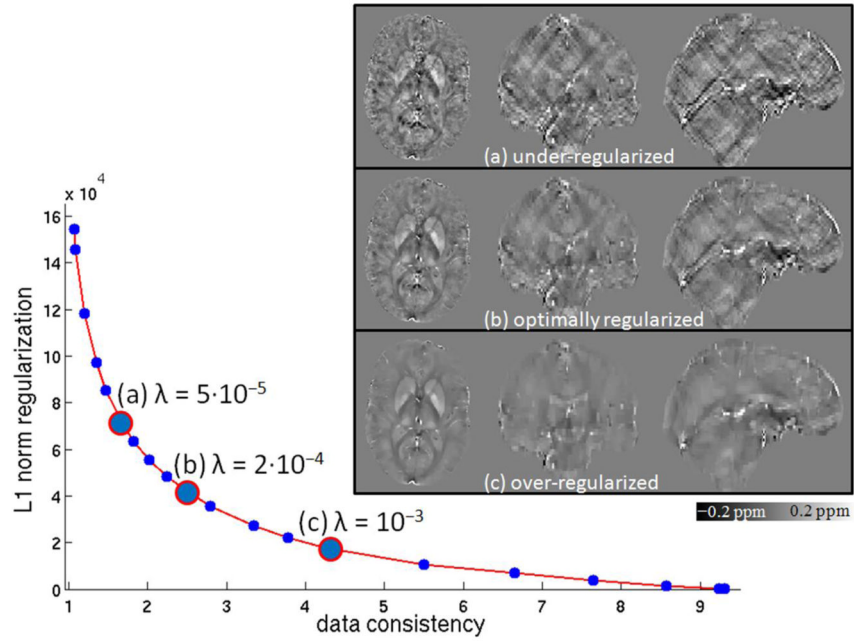


Fig. 1.

L-curve for ℓ_1 -regularized QSM results for a young subject. X-axis: data consistency term $\|\delta - \mathbf{F}^{-1} \mathbf{D} \mathbf{F} \chi\|_2$ in regularized reconstruction for varying values of the smoothing parameter λ . Y-axis: regularization term $\|\mathbf{G} \chi\|_1$. Setting $\lambda = 5 \cdot 10^{-5}$ yielded an under-regularized susceptibility map with ringing artifacts (a), whereas using $\lambda = 10^{-3}$ resulted an over-regularized reconstruction (c). For $\lambda = 2 \cdot 10^{-4}$, the operating point with the largest curvature on the L-curve was obtained (b). This setting was used for the reported ℓ_1 -regularized results.

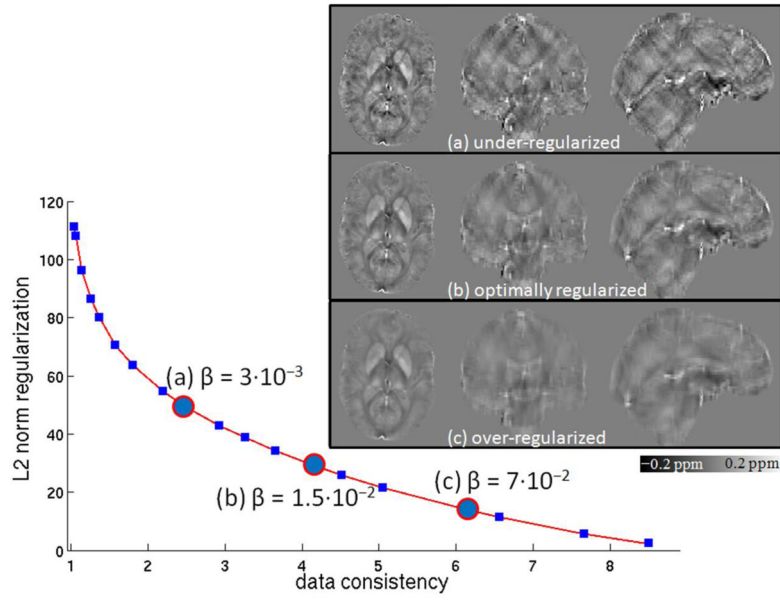


Fig. 2. L-curve for ℓ_2 -regularized QSM results for a young subject. X-axis: data consistency term $\|\delta - \mathbf{F}^{-1} \mathbf{D} \mathbf{F} \chi\|_2$ in regularized reconstruction for varying values of the smoothing parameter β . Y-axis: regularization term $\|\mathbf{G} \chi\|_2$. Setting $\beta = 3 \cdot 10^{-3}$ yielded an under-regularized susceptibility map with ringing artifacts (a), whereas using $\beta = 7 \cdot 10^{-2}$ resulted an over-regularized reconstruction (c). For $\beta = 1.5 \cdot 10^{-2}$, the operating point with the largest curvature on the L-curve was obtained (b). This setting was used for the reported ℓ_2 -regularized results.

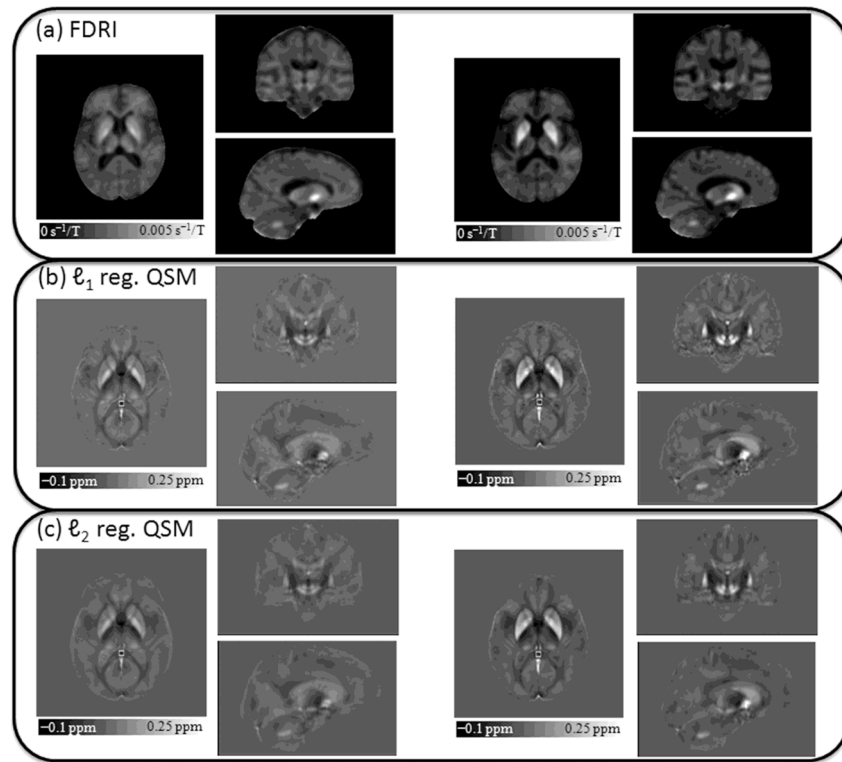


Fig. 3. Young (left) and elderly (right) group averages for FDRI (a), ℓ_1 -regularized QSM (b), and ℓ_2 -regularized QSM (c). Greater iron concentration yields brighter QSM and FDRI images. Splenium reference ROIs are indicated with a white box on the axial QSM slices.

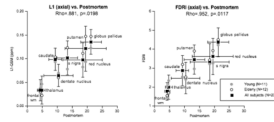


Fig. 4. X-axis: Mean \pm SD iron concentration (mg/100 g fresh weight) determined *postmortem* in each ROI (Hallgren and Sourander, 1958). Y- axis: Mean \pm SD ℓ_1 -regularized QSM in ppm (left) and FDRI in s^{-1} /Tesla (right) indices in all 23 subjects (black squares); the gray circles indicate the mean of the young group, and the open circles indicate the mean of the elderly group.

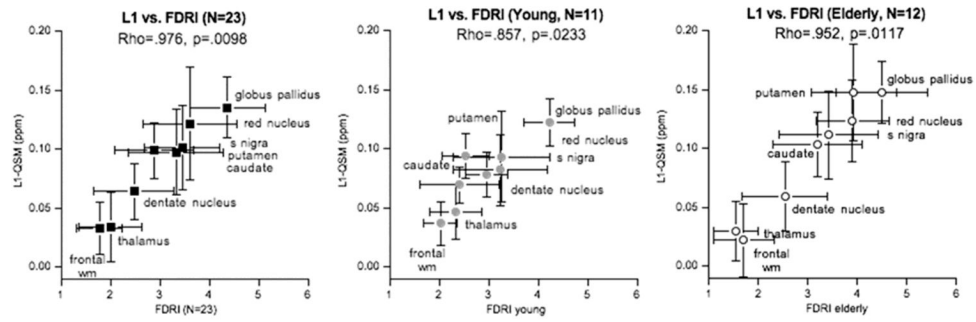


Fig. 5. Correlation between FDRI and ℓ_1 -regularized QSM results on the regions of interest. Results indicate strong relationship between the two methods ($Rho = 0.976$, $p = 0.0098$). Left: all 23 subjects; middle: young group; right: elderly group.

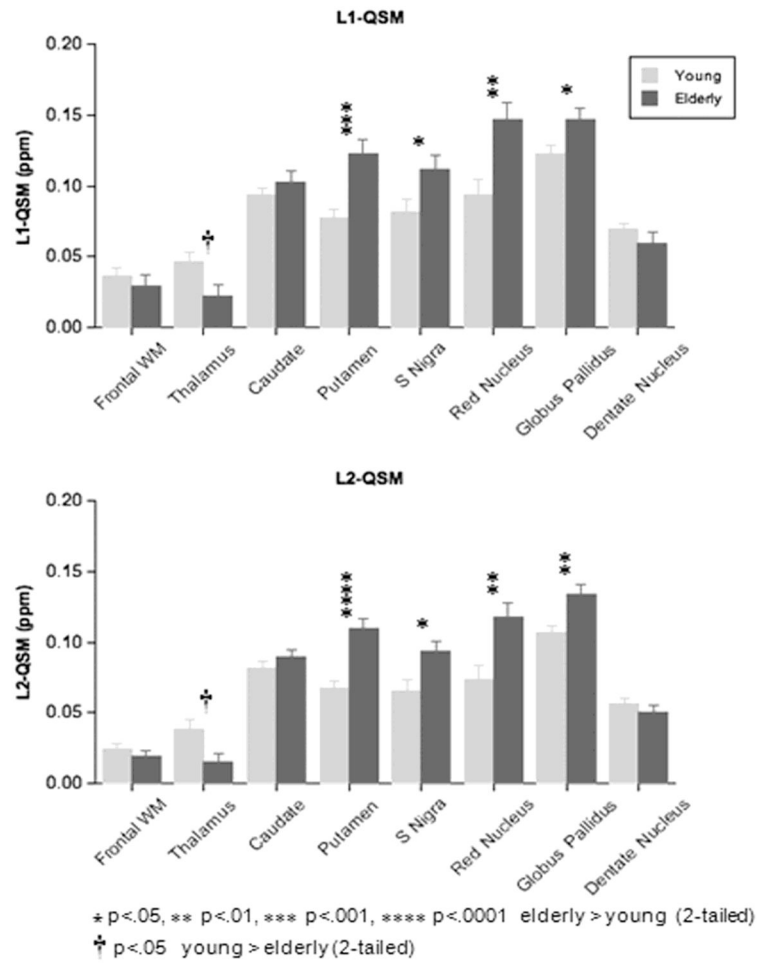


Fig. 6. Mean \pm S.E.M. of average susceptibility in ppm computed by the two methods (ℓ_1 -regularized QSM, top; ℓ_2 -regularized QSM, bottom) for each ROI in the young and elderly groups.

Table 1a

Mean (\pm SD) of each measure by region for each group: ℓ_1 -regularized QSM results using phase-guided ROIs and FDR1-guided ROIs

Region	ℓ_1 -regularized QSM (ppm), phase-guided ROIs		ℓ_1 -regularized QSM (ppm), FDR1-guided ROIs	
	Young (N=11)	Elderly (N=12)	Young (N=11)	Elderly (N=12)
Frontal WM	0.0367 (0.0187)	0.02982 (0.0251)	0.0349 (0.0190)	0.0275 (0.0194)
		<i>t</i> = -0.7505 ^a <i>p</i> = 0.2307		<i>t</i> = -0.9182 ^a <i>p</i> = 0.1844
Thalamus	0.0464 (0.0230)	0.0220 (0.0129)	0.0420 (0.0210)	0.0208 (0.0317)
		<i>t</i> = -2.1336 ^a <i>p</i> = 0.0224		<i>t</i> = -1.8805 ^a <i>p</i> = 0.0370
Caudate	0.0937 (0.0189)	0.1033 (0.0274)	0.0763 (0.0224)	0.1038 (0.0356)
		<i>t</i> = 0.9689 <i>p</i> = 0.1718		<i>t</i> = 2.1970 <i>p</i> = 0.0197
Putamen	0.0779 (0.0188)	0.1233 (0.0343)	0.0683 (0.0205)	0.1134 (0.0369)
		<i>t</i> = 3.8807 <i>p</i> = 0.0004		<i>t</i> = 3.5777 <i>p</i> = 0.0009
Globus Pallidus	0.1224 (0.0200)	0.1472 (0.0261)	0.1422 (0.0172)	0.1961 (0.0318)
		<i>t</i> = 2.5420 <i>p</i> = 0.0095		<i>t</i> = 4.9807 <i>p</i> = 0.0001
Substantia Nigra	0.0820 (0.0299)	0.1113 (0.0372)	0.1045 (0.0426)	0.1524 (0.0331)
		<i>t</i> = 2.0712 <i>p</i> = 0.0254		<i>t</i> = 3.0319 <i>p</i> = 0.0031
Red Nucleus	0.0933 (0.0379)	0.1473 (0.0413)	0.0927 (0.0395)	0.1435 (0.0458)
		<i>t</i> = 3.2568 <i>p</i> = 0.0019		<i>t</i> = 2.8404 <i>p</i> = 0.0049
Dentate Nucleus	0.0693 (0.0151)	0.0595 (0.0292)	0.0544 (0.0174)	0.0487 (0.0225)
		<i>t</i> = -1.0000 ^a <i>p</i> = 0.1643		<i>t</i> = -0.6703 ^a <i>p</i> = 0.2550

p-values are 2-tailed. Numbers in bold indicate significant differences, family-wise Bonferroni corrected based on one-tailed directional hypotheses, requiring $p \leq 0.0125$ for 8 comparisons.

^aNegative *t* values indicate a group difference with the elderly having less iron than the young.

Table 1b

Mean (\pm SD) of each measure by region for each group: ℓ_2 regularized QSM results using phase-guided ROIs and FDR1-guided ROIs

Region	ℓ_2 -regularized QSM (ppm), phase-guided ROIs		ℓ_2 -regularized QSM (ppm), FDR1-guided ROIs	
	Young (N=11)	Elderly (N=12)	Young (N=11)	Elderly (N=12)
Frontal WM	0.0240 (0.0146)	0.0191 (0.0143)	0.0228 (0.0156)	0.0187 (0.0124)
		$t = -0.8163^a$ $p = 0.2118$		$t = -0.7029^a$ $p = 0.2449$
Thalamus	0.0388 (0.0214)	0.0155 (0.0194)	0.0344 (0.0199)	0.0139 (0.0211)
		$t = -2.738^a$ $p = 0.0061$		$t = -2.3931^a$ $p = 0.0131$
Caudate	0.0814 (0.0164)	0.0897 (0.0195)	0.0653 (0.0211)	0.0888 (0.0276)
		$t = 1.1032$ $p = 0.1412$		$t = 2.2814$ $p = 0.0166$
Putamen	0.0677 (0.0168)	0.1101 (0.0248)	0.0568 (0.0176)	0.0976 (0.0264)
		$t = 4.7501$ $p = 0.0001$		$t = 4.3091$ $p = 0.0002$
Globus Pallidus	0.1069 (0.0188)	0.1341 (0.0233)	0.1221 (0.0153)	0.1740 (0.0298)
		$t = 3.0833$ $p = 0.0028$		$t = 5.1724$ $p = 0.0001$
Substantia Nigra	0.0656 (0.0280)	0.0939 (0.0246)	0.0832 (0.0354)	0.1210 (0.0227)
		$t = 2.5812$ $p = 0.0087$		$t = 3.0743$ $p = 0.0029$
Red Nucleus	0.0740 (0.0333)	0.1184 (0.0331)	0.0738 (0.0339)	0.1141 (0.0379)
		$t = 3.2024$ $p = 0.0021$		$t = 2.6751$ $p = 0.0071$
Dentate Nucleus	0.0570 (0.0137)	0.0509 (0.0178)	0.04314 (0.0146)	0.0400 (0.0147)
		$t = -0.9161^a$ $p = 0.1850$		$t = -0.5076^a$ $p = 0.3085$

p-values are 2-tailed. Numbers in bold indicate significant differences, family-wise Bonferroni corrected based on one-tailed directional hypotheses, requiring $p \leq 0.0125$ for 8 comparisons.

^aNegative t values indicate a group difference with the elderly having less iron than the young.

Table 1c
 Mean (\pm SD) of each measure by region for each group: FDRl results using phase-guided ROIs and FDRl-guided ROIs

Region	FDRl (s^{-1} /Tesla), phase-guided ROIs		FDRl (s^{-1} /Tesla), FDRl-guided ROIs		<i>t</i> (elderly>young) <i>p</i>
	Young (N=11)	Elderly (N=12)	Young (N=11)	Elderly (N=12)	
Frontal WM	2.02 (0.3268)	1.545 (0.4522)	<i>t</i> = -2.8643^a <i>p</i> = 0.0093	1.5976 (0.6144)	<i>t</i> = -1.8535 ^a <i>p</i> = 0.0779
Thalamus	2.331 (0.5172)	1.698 (0.6105)	<i>t</i> = -2.6712 ^a <i>p</i> = 0.0143	1.6767 (0.6229)	<i>t</i> = -2.4115 ^a <i>p</i> = 0.0251
Caudate	2.531 (0.4752)	3.198 (0.9042)	<i>t</i> = 2.1812 <i>p</i> = 0.0407	2.9789 (1.0421)	<i>t</i> = 1.3198 <i>p</i> = 0.2011
Putamen	2.954 (0.4282)	3.904 (0.738)	<i>t</i> = 3.7284 <i>p</i> = 0.0012	3.9732 (0.7612)	<i>t</i> = 4.1820 <i>p</i> = 0.0004
Globus Pallidus	4.223 (0.5178)	4.497 (0.9267)	<i>t</i> = 0.8642 <i>p</i> = 0.3972	5.5338 (1.0121)	<i>t</i> = 1.9285 <i>p</i> = 0.0674
Substantia Nigra	3.225 (0.9541)	3.421 (0.9988)	<i>t</i> = 0.4804 <i>p</i> = 0.6359	3.9619 (0.9641)	<i>t</i> = 2.0290 <i>p</i> = 0.0553
Red Nucleus	3.268 (0.9763)	3.932 (0.8528)	<i>t</i> = 1.7415 <i>p</i> = 0.0962	3.99916 (0.7634)	<i>t</i> = 2.5240 <i>p</i> = 0.0197
Dentate Nucleus	2.41 (0.7971)	2.533 (0.8682)	<i>t</i> = 0.3546 <i>p</i> = 0.7264	1.9244 (0.5801)	<i>t</i> = -0.3637 <i>p</i> = 0.7196

p-values are 2-tailed. Numbers in bold indicate significant differences, family-wise Bonferroni corrected based on one-tailed directional hypotheses, requiring $p \leq 0.0125$ for 8 comparisons.

^aNegative *t* values indicate a group difference with the elderly having less iron than the young.